

A semi-empirical model for predicting flexural strength of CNT-reinforced CFRP based on tensile strength and interfacial contributions

To Anh Duc1*, Phan Ngoc Minh2, Bui Hung Thang3

¹Vietnam National Space Center, Vietnam Academy of Science and Technology, 18 Hoang Quoc Viet, Nghia Do, Ha Noi, Viet Nam

² Graduate University of Science and Technology, Vietnam Academy of Science and Technology, 18 Hoang Quoc Viet, Nghia Do, Ha Noi, Viet Nam

³ Institute of Materials Science, Vietnam Academy of Science and Technology, 18 Hoang Quoc Viet, Nghia Do, Ha Noi, Viet Nam

*Email: taduc@vnsc.org.vn

Received: 6 May 2025; Accepted for publication: 27 October 2025

Abstract. A semi-empirical model is proposed to predict the flexural strength of CNTreinforced CFRP composites using tensile strength and CNT concentration as primary inputs. model The incorporates three physically meaningful terms, proportional $\sqrt{w_{\rm CNT}}$, $w_{\rm CNT}$, and $w_{\rm CNT}^{3/2}$, to capture matrix toughening, direct CNT reinforcement, and interfacial efficiency. Model parameters were determined via least-squares regression using experimental data from composites with CNT concentrations up to 0.4 wt%. Validation against independent data (0.5–0.8 wt%) showed strong agreement, with errors consistently below 4%. In addition, the model reflects key trends observed in practice: an increase in tensile strength of approximately 20-25% and in flexural strength of about 30-35% at 0.8 wt% CNTs, relative to the baseline. This formulation offers a balanced compromise between physical realism and predictive simplicity, making it useful for materials selection and mechanical design. Future work will extend the model beyond the saturation point to account for CNT agglomeration, nonlinear interfacial behavior, and morphological effects that emerge at higher loadings.

Keywords: Least-aquare eegression, Semi-empirical modeling, CFRP, CNTs, Flexural strength prediction *Classification numbers*: 2.4.4, 2.9.4

1. INTRODUCTION

The enhancement of mechanical properties in fiber-reinforced composites through nanomaterial incorporation has become a central theme in materials engineering [1-10]. Among various strategies, the addition of carbon nanotubes (CNTs) into carbon fiber-reinforced polymer (CFRP) systems has received sustained attention due to CNTs' extraordinary stiffness, tensile strength, and surface area [11-20]. CFRP, a widely used high-performance structural composite, relies on the synergy between stiff carbon fibers and a tough polymer matrix. While the fibers

contribute to load-bearing capacity, the matrix governs interlaminar shear transfer, crack resistance, and energy dissipation. Enhancing the matrix phase or the fiber—matrix interface can yield considerable improvements in both tensile and flexural behavior. In this context, the introduction of CNTs has proven to be an effective avenue for multiscale reinforcement. When uniformly dispersed, CNTs can bridge microcracks, enhance fiber—matrix adhesion through mechanical interlocking and surface energy effects, and create a secondary load path across phases. These mechanisms collectively improve not only the ultimate strength but also the damage tolerance and fatigue life of the composite. CNTs also alter the rheological and curing behavior of the matrix, potentially influencing void content and resin infiltration, factors critically important for aerospace-grade composites.

Consequently, the role of CNTs in CFRPs extends beyond simple stiffening: they introduce complex, nonlinear enhancements that span multiple scales. Capturing this behavior in a predictive model is essential for enabling rational material design and performance optimization in advanced structural applications. Flexural strength, which reflects a composite's ability to withstand bending-induced failure, is a critical design parameter in aerospace and structural applications. Unlike tensile strength, which is dominated by fiber load-bearing capacity, flexural performance is sensitive to interfacial adhesion, matrix ductility, and shear transfer mechanisms, all of which can be substantially improved by nanoscale fillers like CNTs. Despite this potential, quantitative prediction of flexural strength in CNT-reinforced CFRPs remains a complex task due to the nonlinear and multi-scale nature of interactions among fibers, matrix, and nanofillers.

Prior studies have predominantly employed either empirical curve-fitting approaches or complex micromechanical simulations, yet both fall short of providing a comprehensive explanation for the fundamental mechanisms governing the material's behavior [21-30]. However, there remains a gap between accuracy and practicality. This research aims to bridge that gap through a semi-empirical modeling approach: one that is grounded in physical reasoning but simple enough to be applied using limited experimental inputs. Specifically, this work proposes a closed-form equation for flexural strength prediction based on measurable tensile strength and CNT concentration, incorporating three enhancement terms with distinct physical interpretations. The model is calibrated using a least-squares regression technique and validated over a practical CNT loading range. Emphasis is placed on achieving a balance between accuracy, simplicity, and scientific transparency.

2. MATERIALS AND METHODS

2.1. Materials

CNTs were sourced from Sigma-Aldrich. These nanotubes possess an outer diameter ranging from 50 to 90 nm, with an average diameter of approximately 65 nm as determined by field emission scanning electron microscopy (FE-SEM). The aspect ratio exceeds 100, and the specific surface area is measured at 28 m²/g via nitrogen adsorption techniques. The carbon content is greater than 95% on a carbon basis, with a bulk density of 0.007 g/cm³ and a real density of approximately 2.1 g/cm³. Synthesized through chemical vapor deposition (CVD), these CNTs exhibit a high degree of graphitization, evidenced by a D/G intensity ratio of 0.1 obtained from Raman spectroscopy. Their structural integrity and purity render them suitable for functionalization and incorporation into polymer matrices for advanced material applications.

The carbon fiber reinforcement was a plain-weave bidirectional fabric made from Toray T300 3K continuous carbon filaments. Each fiber bundle (tow) consists of 3,000 filaments, with

a nominal fiber diameter of 7 μ m and areal density of approximately 200 g/m². The T300 fibers exhibit a tensile strength of 3,530 MPa and a Young's modulus of 230 GPa. This fabric is well-suited for manual lay-up processes due to its drapability, uniform surface area, and compatibility with thermoset resin systems.

The matrix system comprises epoxy resin DER-331 and hardener methyl tetrahydrophthalic anhydride (MTHPA), both manufactured by Dow Chemical Company (USA). DER-331 epoxy exhibits an epoxy equivalent weight of 186 g/eq and an epoxy group content of 22.8%. Its viscosity at 25 °C ranges from 110–140 poise, and its density is $1.16 \, \text{g/cm}^3$. The resin contains \leq 700 ppm water and \leq 500 ppm residual epichlorohydrin, with a shelf life of 24 months. The corresponding curing agent, MTHPA, has a molecular weight of 166 g/mol, density of 1.197 g/cm³, and viscosity between 0.58–0.60 poise at 25 °C. It maintains a purity of \geq 99.0% and an acid value \leq 0.5%, with a boiling point of 279 °C. These properties ensure low-viscosity processing, thermal stability, and high mechanical performance after curing, making the system suitable for aerospace-grade CFRP composites.

Analytical-grade nitric acid (HNO $_3$, 70%) and sulfuric acid (H $_2$ SO $_4$, 98%) were procured from Sigma-Aldrich (Merck KGaA, Darmstadt, Germany) for reagent-grade chemical treatments. These high-purity acids are widely employed in laboratory-scale oxidation reactions and surface functionalization of nanomaterials due to their strong oxidative capacity and stable composition.

2.2. Semi-empirical formulation

We propose the following semi-empirical model:

$$\sigma_f = \sigma_t \cdot \left(1 + A \cdot \sqrt{w_{CNT}} + B \cdot w_{CNT} + C \cdot w_{CNT}^{3/2} \cdot \eta_{IF}\right)$$

(1)

Where:

- σ_f is the flexural strength of the composite (MPa);
- σ_t is the tensile strength of the composite (MPa);
- w_{CNT} is the CNT weight fraction expressed as a decimal (e.g., 0.004 for 0.4 wt%);
- η_{IF} is the interfacial efficiency factor (dimensionless), representing the quality of CNT dispersion and bonding at the fiber–matrix interface;
 - A, B, and C are empirical coefficients determined from regression analysis.

The rationale for expressing flexural strength as an amplified form of tensile strength lies in the shared underlying failure mechanisms of CFRP laminates under both loading modes. While tensile strength (σ_t) quantifies the uniaxial load-bearing capacity of the composite, flexural strength (σ_t) arises from a combined state of tension, compression, and interlaminar shear across the cross-section of the specimen. In high-quality CFRPs, those with low porosity, uniform fiber alignment, and strong fiber–matrix bonding, the failure modes under flexure and tension are often fiber-dominated and structurally correlated. As a result, improvements in tensile performance due to the introduction of CNTs are generally mirrored by proportional gains in flexural behavior. This empirical observation justifies modeling σ_f as a scaled version of σ_t , with amplification terms that capture the additional mechanisms active in bending but not fully expressed in tension.

The proposed model therefore introduces three physically motivated enhancement terms. The first term, $A \cdot \sqrt{w_{\rm CNT}}$, captures the nonlinear but significant effect of CNTs embedded within the polymer matrix. This square-root dependence stems from classical fracture mechanics and toughening theories, where reinforcement mechanisms such as crack bridging, CNT pull-out, and local stiffening are shown to scale sub-linearly with filler volume fraction. At low CNT concentrations, the incremental gain in energy dissipation and crack resistance is substantial, but the effect diminishes as the matrix becomes saturated with dispersed nanofillers. The $\sqrt{w_{\rm CNT}}$ scaling accurately reflects this early-stage enhancement followed by gradual saturation.

The second term, $B \cdot w_{\text{CNT}}$, represents the direct contribution of CNTs to fiber-matrix interfacial strength. CNTs aligned or anchored at the interface act as nanoscale shear bridges, enhancing stress transfer between the matrix and carbon fibers. This term assumes linear scaling with CNT content in the absence of agglomeration, consistent with shear-lag theory and experimental studies showing proportional increases in interfacial shear strength with nanoparticle incorporation. It effectively models the strengthening contribution from well-dispersed CNTs that remain mechanically coupled to both phases.

The third term, $C \cdot w_{CNT}^{3/2} \cdot \eta_{IF}$, accounts for cooperative, higher-order mechanisms that arise when CNT content approaches the saturation threshold. The 3/2 power law is intentionally chosen to reflect an intermediate scaling regime, stronger than linear, yet sub-quadratic. As CNTs increase, they begin to exhibit collective behavior: forming local agglomerates, interpenetrating networks, or synergizing with the fiber surface. These interactions increase load-sharing efficiency and strain localization resistance, enhancing flexural strength disproportionately to simple volumetric addition. A quadratic term w_{CNT}^2 would imply unchecked strengthening, which contradicts the well-documented onset of diminishing returns and property degradation beyond saturation. Thus, $w_{CNT}^{3/2}$ captures the optimal regime of cooperative enhancement before negative effects dominate.

Alternative functional forms, including logarithmic, exponential, and saturation-type expressions, were also examined during preliminary modelling. These approaches were ultimately rejected due to their inferior statistical fit to the experimental dataset, their tendency to overestimate flexural strength at low CNT contents or underestimate it near the saturation regime, and their limited correspondence with established physical mechanisms of CNT reinforcement. In particular, the adopted polynomial–power law formulation aligns with micromechanical theories describing sublinear matrix toughening, linear interfacial load transfer, and cooperative effects near saturation. It further provides physically interpretable coefficients while maintaining high predictive accuracy without requiring an excessive number of parameters or curve-specific constants.

The inclusion of η_{IF} , the interfacial efficiency factor, ensures the model remains generalizable. This parameter captures the influence of CNT alignment, dispersion uniformity, and interfacial chemical affinity between the matrix and carbon fibers. In this study, it is assumed that all composite specimens are fabricated with homogeneous CNT distribution, minimal void content, and optimal fiber wetting. Under these controlled conditions, $\eta_{IF}=1$ is justified as it represents an idealized but experimentally achievable interfacial state.

To calibrate the empirical parameters A, B, and C, we adopt the least-squares method, which is widely recognized for producing statistically optimal fits in the presence of measurement noise or model uncertainty. Given that the number of available data points exceeds the number of unknowns, least-squares fitting allows us to determine the best-fitting parameters

that minimize the cumulative squared deviation between predicted and experimental results. In this study, four experimental data points corresponding to CNT concentrations of 0.1%, 0.2%, 0.3%, and 0.4% are used to fit the three unknown parameters. this overdetermined system improves the stability of the regression and guards against local anomalies or fluctuations in individual measurements.

The assumption that σ_f scales from σ_t is grounded in classical beam theory and laminate mechanics: in fibre-dominated CFRP with strong interfaces and low porosity, three-point bending failure initiates when the outer-ply tensile stress approaches the laminate tensile strength, so $\sigma_f \approx \kappa \sigma_t$ with $\kappa > 1$ set by shear transfer and geometry. Because CNTs primarily enhance matrix toughening and fibre-matrix load transfer, the same mechanisms that raise σ_t their influence on bending is well captured by modelling $\sigma_f = \sigma_t [1 + A\sqrt{w_{\rm CNT}} + B w_{\rm CNT} +$ $C w_{\rm CNT}^{3/2}$, where the $\sqrt{w_{\rm CNT}}$, $w_{\rm CNT}$ and $w_{\rm CNT}^{3/2}$ terms respectively reflect sublinear matrix toughening, first-order interfacial strengthening, and cooperative pre-saturation effects. Empirically, our dataset shows tight co-variation of σ_t and σ_f across 0–0.8 wt% CNTs, consistent with a fibre-dominated regime. Beyond ~0.8 wt%, agglomeration and interfacial degradation may emerge; rather than risk over-fitting with unconstrained forms on sparse data, we confine calibration to the effective-dispersion regime and propose a modular extension for future work: $\sigma_f = \sigma_t [1 + A\sqrt{w_{\rm CNT}} + B w_{\rm CNT} + C w_{\rm CNT}^{3/2}] S(w_{\rm CNT})$, where $S(w_{\rm CNT})$ is a saturation/penalty factor (e.g., $S = 1/(1 + (w_{\rm CNT}/w_s)^m)$ or $S = \exp[-\lambda(w_{\rm CNT} - w_s)_+^m]$ or, equivalently, an interfacial-efficiency term $\eta_{IF}(w)$ that decreases beyond a threshold w_s . This preserves interpretability in the validated range while providing a clear path to incorporate degradation once higher-loading data are available.

2.3. Sample preparation

Although CNTs possess remarkable tensile strength, stiffness, and aspect ratio, their tendency to agglomerate due to strong van-der-Waals forces often limits their reinforcing effectiveness. This issue worsens in high-viscosity matrices like epoxy, where dispersion is hindered, leading to poor load transfer and stress concentration. To overcome this, CNTs are typically functionalized to enhance compatibility and dispersion. Carboxyl (-COOH) groups are particularly effective, as they improve solubility in polar media and promote strong interfacial bonding with the matrix, enabling uniform distribution and more efficient stress transfer.

Figure 1 presents the procedure for functionalizing CNTs with carboxyl groups (-COOH) to improve their dispersion and interfacial compatibility. CNTs are first stirred in a mixture of 0.1 mol HNO₃ and 0.3 mol H₂SO₄ for 4 hours, followed by ultrasonication for another 4 hours to promote oxidation and deagglomeration. The resulting Solution A is filtered using vacuum filtration with distilled water to remove residual acids, producing wet CNTs-COOH. After drying for 24 hours, dry functionalized CNTs are obtained. This method enhances CNT surface polarity, promoting better interaction with polar matrices.

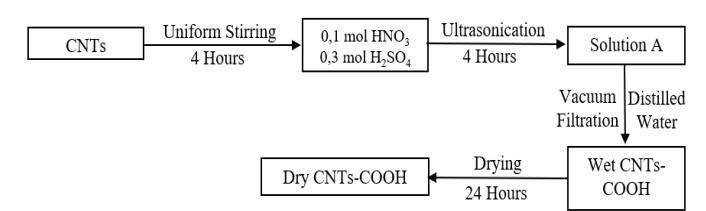


Figure 1. Functionalization Process of CNTs Using Acid Treatment and Ultrasonication

To assess the fundamental structural impact of surface modification on the nanotube framework, spectroscopic and diffraction analyses were conducted prior to evaluating dispersion quality or composite fabrication performance. Raman spectroscopy (Figure 2a) was employed to investigate structural modifications in CNTs before and after chemical functionalization. This technique is particularly effective for assessing the degree of graphitic ordering and the presence of lattice defects by examining characteristic vibrational bands of C-C bonds within the carbon framework. The Raman spectra of pristine CNTs and functionalized CNTs reveal two principal features: the G band (~1,600 cm⁻¹), associated with in-plane stretching of sp²-hybridized carbon atoms in well-ordered graphitic domains, and the D band (~1,340 cm⁻¹), which is indicative of disorder such as defects, grain boundaries, and amorphous carbon regions. In pristine CNTs, the relatively high intensity of the G band compared to the D band reflects a high degree of crystallinity. In contrast, functionalized CNTs display a markedly increased D band intensity, signifying a substantial rise in defect density. This change is attributable to surface functionalization with carboxyl (-COOH) groups, which locally disrupt π -conjugation in the sp² network and introduce sp³-hybridized sites through covalent bonding. The corresponding increase in the D-to-G intensity ratio (I_D/I_G) quantitatively confirms that functionalization has introduced a significant level of structural disorder, thereby validating the successful grafting of functional groups that can enhance interfacial compatibility in composite systems.

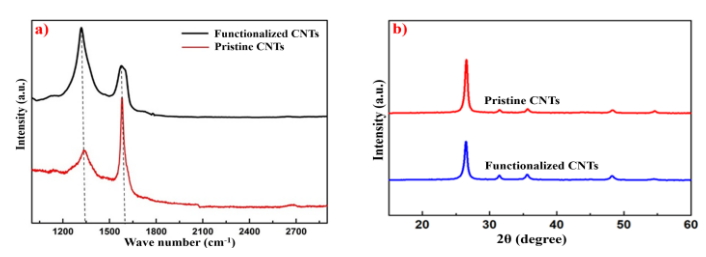
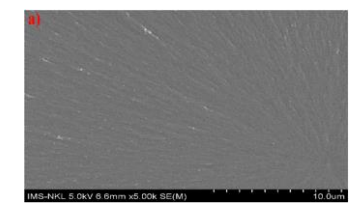


Figure 2. (a) Raman spectra of CNTs and functionalized CNTs; (b) X-ray diffraction patterns of CNTs and functionalized CNTs.

X-ray diffraction (XRD), as shown in Figure 2b, was conducted to examine the crystallographic structure and degree of order in pristine and functionalized CNTs. The diffraction profiles exhibit the characteristic (002) reflection of graphitic materials at approximately $2\theta \approx 26^{\circ}$, corresponding to the interlayer spacing of stacked graphene sheets. Pristine CNTs show a sharp and intense (002) peak, indicative of a high level of structural ordering and well-aligned graphitic layers. Additional weaker reflections at higher angles (~43° and ~53°) correspond to the (100) and (004) planes, consistent with ordered carbon frameworks. Following functionalization, the functionalized CNTs retain these reflections, confirming that the fundamental tubular graphitic framework remains intact. However, two notable changes are observed: (i) the (002) peak intensity decreases slightly, suggesting a modest reduction in crystallinity due to defect introduction, and (ii) peak broadening occurs, which can be associated with interlayer spacing variations or partial disruption of graphitic stacking. These changes are consistent with the covalent attachment of -COOH groups, which locally perturb the lattice while preserving the overall layered morphology. The combined Raman and XRD results provide a coherent picture: surface functionalization increases defect concentration while maintaining the primary graphitic backbone, a balance that is critical for retaining mechanical integrity while enhancing chemical reactivity for advanced material applications.



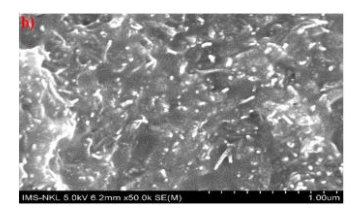


Figure 3. SEM micrographs comparing fracture surfaces of: (a) neat epoxy (5k× magnification) and (b) epoxy reinforced with 0.2 wt% functionalized CNTs (50k× magnification).

Building upon the structural evidence from Raman and XRD analyses, morphological inspection was undertaken to verify whether the chemical functionalization translated into uniform nanoscale distribution within the cured matrix. The effectiveness of the dispersion protocol, acid functionalization followed by prolonged ultrasonication and mechanical stirring, was confirmed by SEM examination of the cured composites. Figure 3a shows the fracture surface of neat epoxy, which is smooth and featureless, while Figure 3b presents the matrix containing 0.1 wt% CNTs. In the latter, CNTs are evident as fine protrusions and embedded fibrils homogeneously distributed across the surface, with no evidence of dense aggregates or void-rich clusters. This uniform distribution, together with the consistent mechanical performance observed across specimens, supports the conclusion that the CNTs were well dispersed at this concentration.

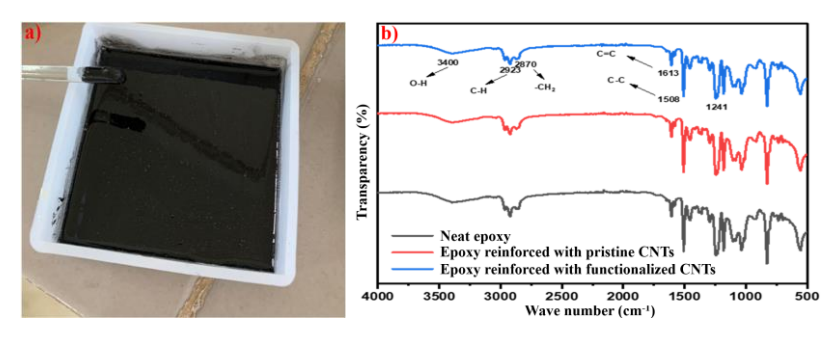


Figure 4. (a) Uniform and well-dispersed distribution of functionalized CNTs within the epoxy matrix. (b) FTIR spectra of neat epoxy, pristine CNTs, and functionalized CNTs.

Following confirmation of nanoscale dispersion in the fracture surface, bulk-scale visual and spectroscopic examinations were performed to corroborate matrix homogeneity and probe potential molecular interactions between the functionalized CNTs and the polymer network. In Figure 4a, the uniformly dark appearance of the mixture attests to the good dispersion of functionalized CNTs within the epoxy matrix, visually reinforcing the nanoscale evidence previously observed in Figure 3b. In that SEM micrograph, CNTs were seen as fine fibrils homogeneously embedded across the fracture surface, with no sign of agglomeration or void-rich regions. This morphological consistency between Figures 3b and 4a reflects the effectiveness of the combined acid functionalization, ultrasonication, and mechanical stirring protocol in breaking down CNT bundles and promoting their interfacial compatibility with the polymer matrix.

Figure 4b presents the FTIR spectra of neat epoxy, epoxy reinforced with pristine CNTs, and epoxy reinforced with functionalized CNTs, offering molecular-level insight into these interactions. All three spectra display the characteristic vibrational modes of epoxy: strong C–H stretching bands at 2,923 cm⁻¹ and 2,870 cm⁻¹ associated with alkyl groups; the aromatic C=C

stretching mode at 1,613 cm⁻¹; primary amine N-H bending in the same region; the intense aromatic C-C stretching vibration at 1,508 cm⁻¹; and the =C-H bending vibration at 1,241 cm⁻¹. The absence of any new absorption peaks across all samples indicates that the chemical backbone of the epoxy remains intact and that no unintended side reactions occurred during CNT incorporation. However, the progressive attenuation of peak intensities from neat epoxy to epoxy/CNTs and epoxy/functionalized CNTs, coupled with the slight broadening of specific bands, most notably those at 1,613 cm⁻¹ and 1,508 cm⁻¹, suggests significant interfacial interactions between the CNTs and the epoxy network. These effects can be attributed to π - π stacking between the CNT sidewalls and the aromatic rings of epoxy, hydrogen bonding involving functional groups introduced during CNT acid treatment, and possible restriction of local chain mobility near the CNT-epoxy interface. Functionalized CNTs, in particular, exhibit stronger suppression of vibrational intensity, likely due to the higher density of polar oxygencontaining groups on their surface, which enhances chemical affinity and stress transfer at the interface. This spectroscopic evidence, in concert with the morphological uniformity observed in Figure 3, underscores the conclusion that functionalized CNTs not only disperse more effectively but also form more intimate molecular interactions with the epoxy matrix, potentially translating into improved macroscopic mechanical performance.

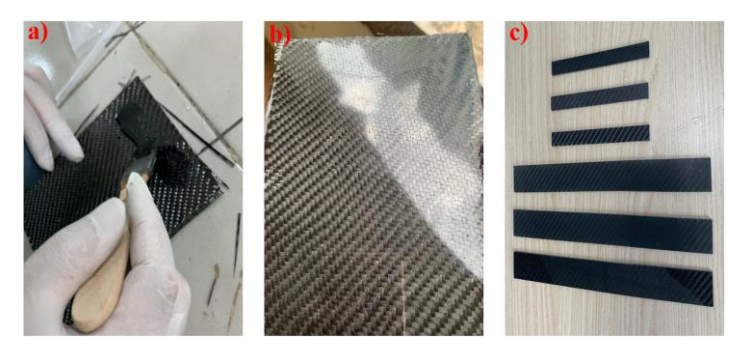


Figure 5. The process of manufacturing tensile and flexural test samples: (a) Hand lay-up of carbon fiber fabric with matrix application; (b) Composite surface after curing; (c) Final specimens cut to standard dimensions for tensile and flexural testing.

With both the nanoscale and bulk dispersion characteristics established, attention was then directed toward the practical integration of functionalized CNTs into composite laminates, documenting each stage from matrix preparation to specimen fabrication. Figure 5 demonstrates the fabrication process beginning with the incorporation of well-dispersed CNTs-COOH into the matrix, resulting in a homogeneous mixture with improved interfacial compatibility. This mixture is then applied to carbon fiber fabric through the hand lay-up technique, ensuring thorough impregnation. The composite laminate undergoes curing at elevated temperatures to promote effective cross-linking and enhance the structural integrity of the matrix. Post-curing, specimens for mechanical testing are prepared according to standardized protocols: tensile strength samples follow ASTM D638, while flexural strength samples adhere to ASTM D790. All specimens are precisely cut using CNC machining to maintain dimensional accuracy and repeatability. Mechanical properties are evaluated using the AGX-50kNVD multifunctional testing system at Institute for Tropical Technology. In order to reduce measurement uncertainty, each mechanical test was performed on three specimens of identical geometry and fabrication conditions. The tensile strength and flexural strength values reported in Tables 1 and 2 represent the arithmetic mean of these three measurements. This averaging procedure was applied consistently to all CNT concentrations in both the calibration and validation datasets.

2.4. Experimental data

In this study, tensile and flexural strengths of CFRP specimens were evaluated across nine CNT concentrations: 0.0%, 0.1%, 0.2%, 0.3%, 0.4%, 0.5%, 0.6%, 0.7%, and 0.8%. Numerous studies have shown that beyond approximately 0.7–1.0 wt%, CNTs tend to agglomerate due to strong van-der-Waals interactions, resulting in poor dispersion, interfacial voids, and localized stress concentrations that can degrade mechanical performance. Additionally, high CNT loading substantially increases the viscosity of the resin, hindering fiber wetting and uniform matrix infiltration. These adverse effects have been widely reported across both thermoset and thermoplastic matrices, including CFRP systems. In this study, the saturation point was conservatively set at 0.8 wt% based on experimental challenges encountered in dispersing CNTs uniformly into the polymer matrix. Furthermore, the objective of this model is to accurately capture the mechanical behavior within the typical reinforcement range. Investigations into agglomeration effects and mechanical performance beyond 0.8 wt% are deferred to future work.

The concentrations of 0.1%, 0.2%, 0.3%, and 0.4% were employed to calibrate the semiempirical model and determine the parameters A, B, and C via least-squares fitting. The remaining data points (0.5%, 0.6%, 0.7%, and 0.8%) were subsequently used to validate the predictive accuracy of the model after the parameters had been established.

2.5. Determination of semi-empirical parameters

Firstly, we transform Equation (1) into a form amenable to linear regression by dividing both sides by σ_t and subtract 1:

$$\frac{\sigma_f}{\sigma_t} - 1 = A \cdot \sqrt{w_{CNT}} + B \cdot w_{CNT} + C \cdot w_{CNT}^{3/2}$$
 (2)

This defines a new variable:

$$\Delta = \frac{\sigma_f}{\sigma_t} - 1 \tag{3}$$

Which becomes the dependent variable in a linear system:

$$\Delta = A \cdot x_1 + B \cdot x_2 + C \cdot x_3 \tag{4}$$

Where: $x_1 = \sqrt{w_{CNT}}$; $x_2 = w_{CNT}$; $x_3 = w_{CNT}^{3/2}$

We then define matrix X and vector Y as follows:

$$X = \begin{bmatrix} \sqrt{w_1} & w_1 & w_1^{\frac{3}{2}} \\ \sqrt{w_2} & w_2 & w_2^{\frac{3}{2}} \\ \sqrt{w_3} & w_3 & w_3^{\frac{3}{2}} \\ \sqrt{w_4} & w_4 & w_4^{\frac{3}{2}} \end{bmatrix} = \begin{bmatrix} \sqrt{0.001} & 0.001 & (0.001)^{3/2} \\ \sqrt{0.002} & 0.002 & (0.002)^{3/2} \\ \sqrt{0.003} & 0.003 & (0.003)^{3/2} \\ \sqrt{0.004} & 0.004 & (0.004)^{3/2} \end{bmatrix}$$

$$Y = \begin{bmatrix} \Delta_1 \\ \Delta_2 \\ \Delta_3 \\ \Delta_4 \end{bmatrix}$$
(6)

CNT Concentration	σ_t (MPa)	σ_f (MPa)	Value of Δ
0.0%	740	775	
0.1%	760	800	$\Delta_1 = 0.0526$
0.2%	780	835	$\Delta_2 = 0.0705$
0.3%	805	870	$\Delta_3 = 0.0807$
0.4%	825	900	$\Delta_4 = 0.0909$

Table 1. Experimental Data and Calculated Δ for Model Calibration

The least-squares solution for A, B, and C is obtained by:

$$\begin{bmatrix} A \\ B \\ C \end{bmatrix} = (X^T X)^{-1} X^T Y \tag{7}$$

which yields: A = 0.098; B = 5.30; C = 41.7

The above results reflect the relative influence of distinct reinforcement mechanisms associated with CNT incorporation in CFRP composites. The small magnitude of A is consistent with the sublinear nature of matrix toughening at low filler content, as expected from fracture mechanics where the benefits of crack-bridging and energy absorption taper off with increased dispersion. The moderate value of B suggests that interfacial load transfer facilitated by CNTs is a more dominant mechanism, particularly in the sub-saturation regime where CNTs are well-aligned and effectively bonded at the fiber—matrix boundary. In contrast, the relatively large value of C highlights the nonlinear amplification effects associated with higher-order interactions, such as CNT clustering, local network formation, or synergistic engagement at the interface, that become increasingly pronounced as the CNT concentration approaches saturation. Importantly, the magnitude of C, although higher, remains within physically reasonable bounds, avoiding the unrealistic exponential scaling that would arise from a purely quadratic formulation. Together, these coefficients demonstrate a coherent and interpretable balance, quantitatively capturing the contributions of dispersed, aligned, and interacting CNTs to the flexural strength of CFRP systems.

Substitute these values back into Equation (1):

$$\sigma_f = \sigma_t \cdot \left(1 + 0.098 \cdot \sqrt{w_{CNT}} + 5.30 \cdot w_{CNT} + 41.7 \cdot w_{CNT}^{3/2}\right) \tag{8}$$

In order to quantitatively assess the fit quality, we calculated the sum of squares of residuals (SSE) by substituting each CNT concentration (w_{CNT} , expressed as a decimal fraction) into the fitted regression equation $\Delta_{\text{pred}} = A\sqrt{w_{CNT}} + Bw_{CNT} + C w_{CNT}^{3/2}$ with A=0.098, B=5.30, and C=41.7. For each calibration point, $\sqrt{w_{CNT}}$, w_{CNT} and $w_{CNT}^{3/2}$ were computed, multiplied by their respective coefficients, and summed to obtain Δ_{pred} ; the residuals were then obtained as the difference between experimental and predicted Δ values. For example, at $w_{CNT} = 0.001$ (0.1% CNT), $\sqrt{w_{CNT}}$, = 0.0316228, $w_{CNT}^{3/2} = 3.16228 \times 10^{-5}$, giving $A\sqrt{w_{CNT}} = 0.03099$, $Bw_{CNT} = 0.00530$, and $C w_{CNT}^{3/2} = 0.001317$, which sum to 0.05259. Subtracting this from the experimental value (0.05260) yields a residual of 1×10^{-5} . The same procedure was applied for all calibration points. The SSE was found to be 1.43×10^{-9} , corresponding to R² (coefficient of determination) being approximately 1.0000, indicating the very good accuracy of the model, The standard errors of the coefficients were 1.3×10^{-4} for A, 0.0100 for B, and 0.59 for C,

confirming the stability of the regression estimates. The regression coefficient estimates were therefore $A = 0.098 \, (\pm 1.3 \times 10^{-4})$, $B = 5.30 \, (\pm 0.0100)$, and $C = 41.7 \, (\pm 0.59)$.

To further assess calibration accuracy, the root mean square error (RMSE) was computed in the physical units of flexural strength (MPa) using RMSE = $\sqrt{\frac{\text{SSE}}{n}}$ after transforming residuals from the Δ -variable scale back to σ_f . For the calibration set, the SSE of 1.43×10^{-9} corresponds to an RMSE of approximately 0.014 MPa, indicating a high degree of alignment between predicted and experimental values within the fitted range. This minimal error is consistent with the $R^2 \approx 1.0000$ value and demonstrates that the functional form accurately captures the physical trends in the calibration regime. Applying the same procedure to the validation dataset yields an RMSE of 24.5 MPa, showing that the model maintains strong predictive capability even outside the fitted concentration range. The marked difference between calibration and validation RMSE arises because the calibration set reflects data the model was explicitly fitted to, whereas the validation set involves higher CNT loadings not used in the fitting; at these concentrations, additional reinforcement or agglomeration mechanisms, absent from the current formulation, introduce larger deviations between predictions and measurements.

For clarity, the calibration can be written in matrix form as $Y = X\beta + \varepsilon$, with $\beta = [A \ B \ C]^{\mathsf{T}}$,

 $Y = [\Delta_1 \ \Delta_2 \ \Delta_3 \ \Delta_4]^{\mathsf{T}}$, and $X = [\sqrt{w_{CNT,i}} \ w_{CNT,i} \ w_{CNT,i}^{3/2}]_{i=1...4}$ is the CNT weight fraction (decimal) and $\Delta_i = \sigma_{f,i}/\sigma_{t,i} - 1$. Using the four calibration points (0.1–0.4 wt% $\rightarrow w_{CNT} = 0.001, 0.002, 0.003, 0.004$), the design matrix and observation vector are:

$$X = \begin{bmatrix} 0.0316228 & 0.0010 & 3.16228 \times 10^{-5} \\ 0.0447214 & 0.0020 & 8.94427 \times 10^{-5} \\ 0.0547723 & 0.0030 & 1.64317 \times 10^{-4} \\ 0.0632456 & 0.0040 & 2.52982 \times 10^{-4} \end{bmatrix}, \qquad Y = \begin{bmatrix} 0.0526 \\ 0.0705 \\ 0.0807 \\ 0.0909 \end{bmatrix}.$$

The overdetermined system was solved by ordinary least squares: $\hat{\beta} = (X^T X)^{-1} X^T Y$ (verified to match a QR-decomposition solution), yielding the reported coefficients. Residuals $r = Y - X\hat{\beta}$ give SSE = $r^T r$ and $R^2 = 1 - \text{SSE}/\sum_i (\Delta_i - \bar{\Delta})^2$; parameter uncertainties follow $\text{Cov}(\hat{\beta}) = \hat{\sigma}^2 (X^T X)^{-1}$ with $\hat{\sigma}^2 = \text{SSE}/(n-p)$ (n = 4, p = 3).

3. RESULTS AND DISCUSSION

Comparison between model prediction (Equation 8) and experimental values, as shown in Table 2, produces errors in the range of -2.42% to -3.73%, with the magnitude of error increasing as CNT concentration rises. This gradual underprediction trend implies that the model, while accurate in the lower loading regime, begins to slightly underestimate the flexural strength at higher CNT contents. This behavior may be attributed to the emergence of physical mechanisms not explicitly modeled, such as the development of a percolated nanotube network, enhanced CNT–fiber synergy, or local interfacial stiffening, which become more pronounced at higher CNT concentrations. Furthermore, these errors reflect the model's conservative nature and its focus on sub-saturation behavior. They also underscore the importance of incorporating more advanced interfacial or morphological descriptors in future iterations of the model.

The dataset also reveals a notable enhancement in mechanical performance with CNT incorporation: at 0.8 % CNT content, tensile strength increases by 20 %, from a baseline of 740 MPa to 887 MPa. Meanwhile, flexural strength rises by 35 %, from 775 MPa to 1,046 MPa.

These gains underscore the reinforcing efficacy of CNTs, particularly under bending loads. The more pronounced improvement in flexural strength aligns with established findings in the literature, which attribute such behavior to the greater influence of nanofillers on matrix-dominated shear and bending mechanisms. This differential response suggests that flexural strength is more sensitive to enhancements in interfacial bonding, matrix toughening, and energy dissipation pathways introduced by CNTs.

CNT Concentration	σ_t (MPa) (Experimental Data)	σ_f (MPa) (Experimental Data)	σ_f (MPa) (Model Prediction)	Error
0.5%	845	950	927	-2.42%
0.6%	865	990	960	-3.03%
0.7%	880	1,025	992	-3.22%
0.8%	887	1,046	1,007	-3.73%

Table 2. Model Validation Using Experimental Data Beyond Calibration Range

To situate the present formulation within the literature, we note that existing approaches largely fall into three categories: (i) purely empirical curve-fits that map σ_f to CNT content using low-order polynomials or sigmoidal "saturation" laws; (ii) micromechanical or shear-lag models that require microstructural inputs not routinely measured in practice; and (iii) multiscale/atomistic simulations that yield mechanistic insight but not compact, design-ready predictors. In contrast, our closed-form relation $\sigma_f = \sigma_t \left[1 + A \sqrt{w_{CNT}} + B w_{CNT} + C w_{CNT}^{3/2} \right]$ links flexural strength to a readily measurable quantity σ_t interfacial load transfer, and cooperative pre-saturation effects, achieving sub-4% validation error over 0.5-0.8 wt% CNTs with only three parameters. Unlike the impact-focused empirical-numerical study in [19], which does not provide a predictor for static flexural strength versus CNT content, and unlike the atomistic interface analysis in [26], whose fidelity comes at the cost of direct applicability, the present semi-empirical model strikes a balance between physical transparency and practical utility, enabling rapid, data-light prediction while remaining grounded in established reinforcement mechanisms. Moreover, compared to the nanoparticle-reinforced epoxy coating investigation in [21], where property gains are attributed to dispersion quality and agglomeration control but no explicit strength-content model is derived, our formulation delivers a direct quantitative link between filler loading and flexural performance. Similarly, while molecular dynamics studies such as [23] and [25] have elucidated nanoscale interfacial strengthening pathways for CNT- and nanoparticle-modified adhesives, often highlighting synergistic effects of hybrid fillers, these works remain confined to atomistic scales and do not yield closed-form, design-ready predictors. The experimental-simulation framework in [24] demonstrates substantial flexural and shear strength gains in CF/PEEK-Ti laminates via GNP incorporation, paralleling our emphasis on interfacial load transfer, yet it focuses on thermoplastic-based fibre-metal laminates rather than thermoset CFRPs. The cohesive-zone modeling of nano-enhanced FRP systems in [27] and the multiscale nanoparticle toughening analysis in [28] each underscore the role of interfacial properties, particle size, and dispersion state in suppressing crack initiation and propagation, mechanistic themes that our model subsumes into the $\sqrt{w_{CNT}}$, w_{CNT} , and $w_{CNT}^{3/2}$ scaling terms, but in a form calibrated directly against macroscale flexural data. Taken together, these comparisons affirm that while the literature provides valuable mechanistic and multiscale insights, our contribution is to distill these into a compact, physically interpretable, and

experimentally validated equation that bridges the gap between nanoscale mechanisms and engineering-scale property prediction.

4. CONCLUSIONS

In this study, a semi-empirical model has been successfully developed to predict the flexural strength of CNT-reinforced CFRP composites using tensile strength and CNT concentration as the primary inputs. This model achieves a high degree of predictive accuracy, with validation errors consistently remaining below 4% across a practical range of CNT concentrations, up to the experimentally supported saturation threshold of 0.8 wt%. Such precision highlights the robustness and applicability of the model in engineering contexts where reliable property estimation is essential. A key feature of the model is the use of a least-squares regression method to calibrate three empirical parameters, providing a statistically optimal fit to experimental data. Moreover, the model formulation incorporates physically meaningful terms, $\sqrt{w_{\rm CNT}}$, $w_{\rm CNT}$, and $w_{\rm CNT}^{3/2}$, that reflect the nonlinear contributions of CNT content to matrix reinforcement, direct load transfer, and interfacial efficiency. These terms collectively encapsulate the key factors governing flexural strength enhancement in CNT-modified CFRPs, especially within the low-to-moderate loading regime where dispersion remains effective. Importantly, the model strikes a balance between simplicity and physical accuracy, avoiding overfitting while maintaining predictive utility. It offers a practical framework for designing and optimizing CNT-reinforced CFRPs in aerospace and structural applications.

Future work will focus on extending the model beyond the current saturation point, where agglomeration and higher-order interactions begin to dominate. Additional refinement may also target further reduction of prediction error and the incorporation of dispersion state, CNT morphology, and multi-scale interfacial phenomena.

Acknowledgements. The authors gratefully acknowledge the financial support provided by Vietnam Academy of Science and Technology (VAST) under Grant Number CSCL39.01/25-26.

CRediT authorship contribution statement. Author 1: Conceptualization, Methodology, Investigation, Writing – original draft.. Author 2: Formal analysis, Writing – review & editing.. Author 3: Funding acquisition, Supervision.

Declaration of competing interest. The authors declare that they have no known competing financial interests or personal relationships that could have appeared to influence the work reported in this paper.

REFERENCES

- 1. Halvaeyfar M. R., Gorji Azandariani M., Zeighami E., Mirhosseini S. M. Retrofitting fiber-reinforced concrete beams with nano-graphene oxide and CFRP sheet: an experimental study, Arch. Civ. Mech. Eng. **25** (1) (2025) 1-21. https://doi.org/10.1007/s43452-024-01093-3
- 2. Anish V., Logeshwari J. A review on ultra high-performance fibre-reinforced concrete with nanomaterials and its applications, J. Eng. Appl. Sci. **71** (1) (2024) 25. https://doi.org/10.1186/s44147-023-00357-8
- 3. Raja T., Devarajan Y. Development of hemp fiber-reinforced epoxy composite with cobalt oxide nanoparticles for fuel cell and energy storage applications, Results Eng. 25 (2025) 103839. https://doi.org/10.1016/j.rineng.2024.103839

- 4. Musa A. A., Bello A., Adams S. M., Onwualu A. P., Anye V. C., Bello K. A., Obianyo I. I. Nano-Enhanced Polymer Composite Materials: A Review of Current Advancements and Challenges, Polymers 17 (7) (2025) 893. https://doi.org/10.3390/polym17070893
- 5. Aikins S. A., Yeboah F. A. B., Enyejo L. A., Kareem L. A. The Role of Thermomechanical and Aeroelastic Optimization in FRP-Strengthened Structural Elements for High-Performance Aerospace and Civil Applications, Int. J. Sci. Res. Mech. Mater. Eng. **9** (1) (2025) 35-65. https://doi.org/10.32628/IJSRMME25144
- 6. Rashid A. B., Haque M., Islam S. M., Labib K. R. U. Nanotechnology-enhanced fiber-reinforced polymer composites: Recent advancements on processing techniques and applications, Heliyon **10** (2) (2024). https://doi.org/10.1016/j.heliyon.2024.e24692
- 7. Dejene B. K. Advancing natural fiber-reinforced composites through incorporating ZnO nanofillers in the polymeric matrix: a review, J. Nat. Fibers **21** (1) (2024) 2356015. https://doi.org/10.1080/15440478.2024.2356015
- 8. Dejene B. K. Exploring the potential of ZnO nanoparticle-treated fibers in advancing natural fiber reinforced composites: a review, J. Nat. Fibers **21** (1) (2024) 2311304. https://doi.org/10.1080/15440478.2024.2311304
- 9. Salman A., Hassan A., Ahmed H. I. Effects of steel fibers and carbon nanotubes on the flexural behavior of hybrid GFRP/steel reinforced concrete beams, Beni-Suef Univ. J. Basic Appl. Sci. **13** (1) (2024) 1-18. https://doi.org/10.1186/s43088-024-00584-9
- 10. Srinivasa Perumal K. P., Selvarajan L., Mathan Kumar P., Shriguppikar S. Enhancing mechanical and morphological properties of glass fiber reinforced epoxy polymer composites through rutile nanoparticle incorporation, Prog. Addit. Manuf. **10** (1) (2025) 831-848. https://doi.org/10.1007/s40964-024-00675-0
- Demircan O., Ibrahim M. H. I., Xiao Z. X., Yang J., Li Q., Wang Z. B., Liu Z. Y., Xiao B. L., Zheng Y. G. Effect of heat treatment on microstructure, mechanical property and corrosion resistance of a novel Na₂MoO₄@ CNT/2024 composite, J. Alloys Compd. 1021 (2025) 179607. https://doi.org/10.1016/j.jallcom.2025.179607
- 12. Imran M., Amjad H., Khan S., Ali S. Machine learning assisted prediction of the mechanical properties of carbon nanotube-incorporated concrete, Struct. Concr. **26** (2) (2025) 1613-1635. https://doi.org/10.1002/suco.202400727
- 13. Karimi S. Investigating the durability of nano-reinforced CFRP-aluminum and CFRP-CFRP bonded and bonded/bolted joints under hygrothermal conditions, Polym. Compos. **46** (5) (2025) 4075-4095. https://doi.org/10.1002/pc.29225
- 14. Electric field-assisted alignment of carbon nanotubes in the interlayers of CFRP composites to enhance the properties, Compos. Part A Appl. Sci. Manuf. **190** (2025) 108706. https://doi.org/10.1016/j.compositesa.2024.108706
- 15. Xing F., He Z., Wang S., Gu Y., Han J., Wang Y., Li M. Nano-particles doped carbon nanotube films for in-situ monitoring of temperature and strain during the processing of carbon fiber/epoxy composites, Polym. Compos. **46** (1) (2025) 193-207. https://doi.org/10.1002/pc.28978
- 16. Nurguzhin M., Janikeyev M., Omarbayev M., Yermakhanova A., Meiirbekov M., Zhumakhanov M., Yerezhep D. Structure and Properties of Al–CNT-Based Composites Manufactured by Different Methods: A Brief Review, Materials **18** (1) (2025) 214. https://doi.org/10.3390/ma18010214

- 17. Weng Y., Wu L., Ou Y., Mao D. Short carbon nanotubes: from matrix toughening to interlaminar toughening of CFRP composites, Compos. Commun. **41** (2023) 101652. https://doi.org/10.1016/j.coco.2023.101652
- 18. Kavitha S. S., Joseph L., Kumar P. S., Sarker P. K., Madhavan M. K., Jayanarayanan K. Implementation of multi-walled carbon nanotube incorporated GFRP as an alternative for CFRP in strengthening of concrete cylinders, Struct. **70** (2024) 107606. Elsevier. https://doi.org/10.1016/j.istruc.2024.107606
- 19. Ghosh P., Ramajeyathilagam K. Experimental and numerical investigation on Multiwalled carbon nanotubes (MWCNTs) dispersed CFRP laminate subjected to spherical and conical impacts, Ships Offshore Struct. **19** (12) (2024) 2024-2039. https://doi.org/10.1080/17445302.2024.2317660
- 20. Liu J., Yang T., Wang B., Yu Z., Yang Y., Sun G. Mechanical improvement of carbon fiber/epoxy composites by sizing functionalized carbon nanotubes on fibers, Polym. Compos. **45** (12) (2024) 10645-10653. https://doi.org/10.1002/pc.28497
- 21. Xu L. Y., Wang X. Y., Lin Y. Z., Huang Y., Tao C. C., Zhang D. W. Experimental and numerical investigations of carbon-based nanoparticle reinforcement on microstructure and mechanical properties of epoxy coatings, Chin. J. Polym. Sci. **43** (1) (2025) 211-224. https://doi.org/10.1007/s10118-025-3252-7
- 22. Rahimijonoush A., Mohammadimehr M. The effect of nanoparticles on cold roll bonded fiber metal laminates under high-velocity impact: experimental and numerical approaches, J. Braz. Soc. Mech. Sci. Eng. **47** (4) (2025) 183. https://doi.org/10.1007/s40430-025-05486-0
- 23. Li Y., Li H., Song C., Zhu Z., Ma X. Molecular dynamics simulations of the micro mechanism of functionalized SiO2 nanoparticles and carbon nanotubes modified epoxy resin adhesives, Polym. Compos. **46** (2) (2025) 1587-1603. https://doi.org/10.1002/pc.29059
- 24. Cao M., Wang S., Zang J., Liu M., Qian C., Zhang Y., Na D. Experimental and simulation analysis of the effect of GNPs on the mechanical and interfacial properties of CF/PEEK-Ti fiber metal laminates, Compos. Sci. Technol. **246** (2024) 110387. https://doi.org/10.1016/j.compscitech.2023.110387
- 25. Wang, T., Shi, C., Huang, P., Yang, J., Oeser, M., Liu, P. Experimental characterization and modeling of carbon nanotubes modified epoxy mixture: Electrical and mechanical performance. Construction and Building Materials, **471** (2025) 140752. https://doi.org/10.1016/j.conbuildmat.2025.140752
- 26. Zhang M., Yu Y., Luan Y., Zhou H., Peng X., Gong L., Zhou H. Effects of CNT microstructural characteristics on the interfacial enhancement mechanism of carbon fiber reinforced epoxy composites via molecular dynamics simulations, Thin-Walled Struct. **195** (2024) 111413. https://doi.org/10.1016/j.tws.2023.111413
- 27. Ascione F., De Maio U., Greco F., Lonetti P., Sgambitterra G., Pranno A. Failure analysis of RC structures retrofitted with nano-enhanced FRP systems, Procedia Struct. Integr. **47** (2023) 460-468. https://doi.org/10.1016/j.prostr.2023.07.078
- 28. Chang W., Rose L. F., Sha Z., Huang F., Kinloch A. J., Wang C. H. Multiscale modelling of nanoparticle toughening in epoxy: Effects of particle-matrix interface, particle size, and volume fraction, Compos. Sci. Technol. **256** (2024) 110788. https://doi.org/10.1016/j.compscitech.2024.110788

- 29. Ghosh P., Ramajeyathilagam K. Experimental and numerical investigations on the effect of MWCNT-COOH and Al₂O₃ hybrid nanofillers dispersed CFRP laminates subjected to projectile impact, Processes **11** (5) (2023) 1435. https://doi.org/10.3390/pr11051435
- 30. Shaki M. H., Rostamiyan Y., Seyyedi S. M. Three-point bending performance of circular-shaped core foam-filled sandwich panels reinforced with carbon fibers and silica nanoparticles, Funct. Compos. Struct. **7** (2) (2025) 025001. https://doi.org/10.1088/2631-6331/adc9f9